

Analysis of supershear transition regimes in rupture experiments: the effect of nucleation conditions and friction parameters

Xiao Lu,¹ Nadia Lapusta² and Ares J. Rosakis¹

¹Graduate Aeronautical Laboratories, California Institute of Technology, Pasadena, CA 91125, USA

²Division of Engineering and Applied Science and Division of Geological and Planetary Sciences, California Institute of Technology, Pasadena, CA 91125, USA. E-mail: lapusta@its.caltech.edu

Accepted 2009 January 5. Received 2009 January 3; in original form 2008 April 12

SUMMARY

We consider the effect of the rupture initiation procedure on supershear transition of Mode II ruptures on interfaces governed by linear slip-weakening friction. Our study is motivated by recent experiments, which demonstrated the transition of spontaneous ruptures from sub-Rayleigh to supershear speeds in the laboratory. In these works the experiments were analysed using the Burridge–Andrews model of supershear transition, in which a supershear daughter crack is nucleated in front of the main mother rupture. It was concluded that the critical slip of the linear slip-weakening formulation needs to be pressure-dependent for a good match with experiments. However, the dynamic rupture initiation mechanism in the experiments was conceptually different from the quasi-static one adopted in the numerical work used for comparison. Here, our goal is to determine the effect of the nucleation by numerically modelling the experiments using a rupture initiation procedure that captures the dynamic nature of the wire explosion mechanism used in the experiments. We find parameter regimes that match the experimentally observed transition distances for the entire range of experimental conditions. Our simulations show that the dynamic rupture initiation procedure significantly affects the resulting transition distances, shortening them by about 30–50 per cent compared to those predicted through the quasi-static rupture initiation process. Moreover, for some cases, the dynamic initiation procedure changes the very mode of transition, causing a direct supershear transition at the tip of the main rupture instead of the mother–daughter mechanism. We find reasonable parameter regimes which match experimentally determined transition distances with both direct supershear transition at the rupture tip and the Burridge–Andrews (mother–daughter) mechanism, using both pressure-independent and pressure-dependent critical slip. The results show that there are trade-offs between the parameters of the rupture initiation procedure and the properties of interface friction. This underscores the importance of quantifying experimental parameters for proper interpretation of the experiments and highlights the importance of the rupture initiation procedure, in simulations of both experiments and real-life earthquake events.

Key words: Earthquake dynamics; Rheology and friction of fault zones; Dynamics and mechanics of faulting; Fractures and faults; Mechanics, theory, and modelling.

1 INTRODUCTION

Rupture transition from sub-Rayleigh to supershear speeds (also called ‘supershear transition’) has been the subject of many theoretical and numerical investigations (e.g. Burridge 1973; Andrews 1976; Das & Aki 1977; Burridge *et al.* 1979; Freund 1979; Day 1982; Broberg 1989; Needleman & Rosakis 1999; Abraham & Gao 2000; Madariaga & Olsen 2000; Gao *et al.* 2001; Geubelle & Kubair 2001; Dunham & Archuleta 2005; Festa & Vilotte 2006; Rosakis *et al.* 2007, and references therein; Liu & Lapusta 2008; Shi *et al.* 2008). The occurrence of this phenomenon has been inferred from

seismic observations of large earthquakes (Archuleta 1984; Olsen *et al.* 1997; Bouchon *et al.* 2001; Bouchon & Vallee 2003; Dunham & Archuleta 2004; Ellsworth *et al.* 2004; Robinson *et al.* 2006; Das 2007), and the possibility of such transition has been confirmed in the laboratory (Rosakis *et al.* 1999; Rosakis 2002; Xia *et al.* 2004; Lu *et al.* 2007; Rosakis *et al.* 2007). In particular, Xia *et al.* (2004) reported the first direct observations of supershear transition in rupture experiments designed to mimic crustal earthquakes. Studies of supershear transition have important practical implications. Supershear ruptures can cause much stronger shaking farther from the fault than subsonic ruptures (Aagaard & Heaton 2004; Bernard &

Baumont 2005; Dunham & Archuleta 2005; Bhat *et al.* 2007), as Mach fronts generated by supershear ruptures carry large stresses and particle velocities far from the fault. In addition, understanding which fault properties and conditions do and do not favour supershear transition would allow to constrain properties and conditions on natural faults.

The current study is motivated by the experiments described in Xia *et al.* (2004) and Rosakis *et al.* (2007). Our aim is to understand the possible scenarios of supershear transition in the experiments, and hence to facilitate both the interpretation of the existing experiments and the design of new ones. In the experiments, the Earth's crust was simulated by a square (150 × 150 mm) photo-elastic plate cut to introduce a frictional interface inclined at the angle $\alpha = 25^\circ$ to the horizontal (Fig. 1). Uniform pressure P was applied at the top and bottom ends of the plate, inducing shear traction $\tau_0 = P \sin \alpha \cos \alpha$ and normal traction $\sigma_0 = P \cos^2 \alpha$ on the interface. The ratio of shear to normal tractions, $f_0 = \tau_0/\sigma_0 = \tan \alpha = 0.47$, was smaller than the static friction coefficient $f_s = 0.6$ of the interface, and hence the interface simulated a tectonically loaded fault locked due to friction. A series of experiments was done, with P varying from 8.8 to 15 MPa. Initiation of spontaneous dynamic rupture was achieved by means of an exploding wire acting in the middle of the plate interface across the entire plate thickness. The experiments were done using a photo-elastic material, which allowed to capture and analyse rupture progression using high-speed photography. The images revealed a bilateral spontaneous dynamic shear rupture propagating along the interface, initially with sub-Rayleigh speeds and then transitioning to supershear speeds. The details of the experimental set up, exploding wire mechanism, and optical diagnostics are described in Rosakis *et al.* (2007).

Xia *et al.* (2004) reported the transition distance for each experiment, that is, the distance between the rupture initiation region and the position of the rupture tip when the rupture transitioned to a supershear speed, and compared these transition distances with the ones in the numerical study by Andrews (1976). The numerical work of Andrews (1976), building upon an earlier analytical study of Burridge (1973), showed that supershear transition can be achieved by nucleating a supershear daughter crack ahead of the main rupture, which immediately propagates at a supershear speed and also spreads backwards to unite with the main rupture. This mechanism is often referred to as the Burridge–Andrews mecha-

nism (Rosakis 2002) or the mother–daughter mechanism (Abraham & Gao 2000). Andrews (1976) assumed linear slip-weakening friction, in which the shear strength of the interface decreases linearly from static frictional strength level of τ_s to the dynamic frictional strength level of τ_d over the critical slip D_c , and then remains at τ_d during subsequent sliding (Fig. 1). Using this model, he demonstrated that the transition distance depends only on the critical crack half-length L_c and the seismic ratio s as follows:

$$L = F(s)L_c, \quad L_c = \frac{\mu(\tau_s - \tau_d)D_c}{\pi(1 - \nu)(\tau_0 - \tau_d)^2}, \quad s = \frac{\tau_s - \tau_0}{\tau_0 - \tau_d}. \quad (1)$$

In eq. (1), $F(s)$ is a numerically determined function that can be approximated by $F(s) = 9.8(1.77 - s)^{-3}$ as discussed by Rosakis *et al.* (2007). The parameters μ and ν are the shear modulus and Poisson's ratio of the elastic solid and τ_0 is the initial resolved shear stress acting on the interface. In terms of the geometry of Fig. 1, eq. (1) can be expressed as (Rosakis *et al.* 2007):

$$L = F(s) \frac{\mu(f_s - f_d)D_c}{\pi(1 - \nu)(\sin \alpha - f_d \cos \alpha)^2 P} \propto \frac{1}{P}, \quad s = \frac{f_s - \tan \alpha}{\tan \alpha - f_d}, \quad (2)$$

where $f_s = \tau_s/\sigma_0$ and $f_d = \tau_d/\sigma_0$ are the static and dynamic friction coefficients, respectively. Eq. (2) predicts that the experimentally observed transition distance L should be proportional to P^{-1} , assuming that critical slip D_c does not depend on the far-field compression level P .

The experimentally determined transition distances of Xia *et al.* (2004) were indeed smaller for larger values of P , in qualitative agreement with the results of Andrews (1976). However, the dependence was stronger than P^{-1} . Xia *et al.* (2004) explained the discrepancy by introducing the dependence of critical slip D_c on compression P as $D_c \propto P^{-1/2}$, based on experiments of Ohnaka (2003) and a micromechanical model described in detail by Rosakis *et al.* (2007). The resulting scaling $L \propto P^{-3/2}$ provided a better match with the experimental measurements, as shown in the following sections. While the main contribution of the work by Xia *et al.* (2004) was the demonstration that spontaneous supershear transition is possible, the comparison of the experimental measurements with the theory of Andrews (1976) provided additional insights, pointing to the daughter-crack mechanism as the likely explanation and suggesting that the critical slip D_c is pressure-dependent and that $L \propto P^{-3/2}$.

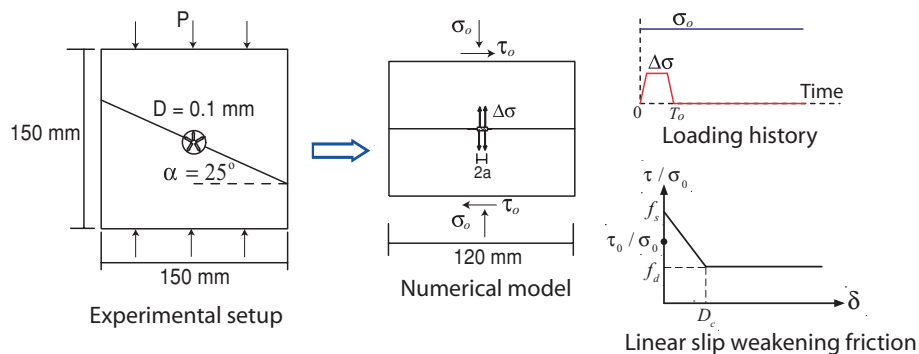


Figure 1. Our model for simulations of supershear transition. Motivated by the experimental set up of Xia *et al.* 2004 (left-hand panel), we consider a planar interface in a thin plate (middle panel). The interface is pre-stressed both in compression, with $\sigma_0 = P \cos^2 \alpha$, and in shear, with $\tau_0 = P \sin \alpha \cos \alpha$. For $\alpha = 25^\circ$ used in the experiments, $\tau_0/\sigma_0 = 0.47$. The rupture is initiated by applying a transient reduction $\Delta\sigma$ of normal stress in the region of length $2a$ in the middle of the interface for time T_0 . The time dependence of the normal-stress reduction is shown in the top of the right-hand panel. The interface is governed by linear slip-weakening friction (bottom of the right-hand panel) with the static coefficient $f_s = 0.6$. Several values of the dynamic friction coefficient f_d and critical slip D_c are considered.

To further analyse the experiments of Xia *et al.* (2004), we conduct extensive numerical simulations to elucidate the effect of the rupture nucleation procedure. The mechanisms of rupture initiation in the experiments of Xia *et al.* (2004) and in the numerical simulations of Andrews (1976) are conceptually different. Our goal is to determine how much the comparison between experimental and numerical results is affected when we consider a numerical model with a nucleation procedure which is closer to the experimental one. In the experiments, the initiation of dynamic rupture was achieved by a local explosion of a thin (0.08 mm in diameter) nickel wire. The wire was embedded within a tunnel (cylindrical hole) of 0.1 mm in width located in the middle of the plate interface and piercing the entire plate thickness. The ends of the wire were connected to a charged capacitor. Following a sudden discharge, the nickel wire was heated by the current surge and turned into high-pressure plasma, relieving the applied compression locally. This allowed shear ruptures to initiate around the explosion site under the action of the resolved shear stress. In contrast, Andrews (1976) used a rupture initiation procedure intended to model smooth rupture acceleration from its critical size $2L_c$. Hence the initiation procedures had two key differences: The initiation procedure in the experiments was (i) relatively abrupt with likely importance of inertial effects and (ii) the same in intensity, rise time, and spatial extent for all compression loads P , while the initiation procedure in the Andrews' model was (1) smooth and quasi-static and (2) dependent on L_c and hence varied with the level of the far-field load P . The potential influence of rupture initiation on subsequent rupture propagation and supershear transition was highlighted in some recent studies (Festa & Vilotte 2006; Shi & Ben-Zion 2006; Ampuero & Ben-Zion 2008; Liu & Lapusta 2008; Shi *et al.* 2008). However, this factor was not considered in the original analysis by Xia *et al.* (2004). Details of rupture initiation may affect transition distances and, in particular, may offer an alternative explanation for the stronger dependence of transition distances on the far-field compression P . Our model, including the initiation mechanism, is described in Section 2.

In terms of friction properties, one parameter in particular seems to be of determining influence on supershear transition in the context of the work by Xia *et al.* (2004). The study of Andrews (1976) showed that transition distances strongly depend on the seismic ratio s . For the experiments of Xia *et al.* (2004), the seismic ratio s is given by (2) with $f_s = 0.6$ and $\alpha = 25^\circ$, resulting in

$$s = 0.13/(0.47 - f_d). \quad (3)$$

Hence transition distances strongly depend on the dynamic friction coefficient f_d which is not precisely known for the Homalite interfaces used in the experiments. Xia *et al.* (2004) used $f_d = 0.2$ in their analysis, based on an additional set of experiments in which they started with a near-horizontal interface ($\alpha = 10^\circ$) and increased the inclination angle until the explosion-induced rupture was able to propagate through the entire sample. Based on the tangent of that critical angle, they estimated that $f_d = 0.2$, which results in $s = 0.5$ and $L/L_c = 4.8$ according to eq. (1). Hence, for $f_d = 0.2$, the transition distance L is only about five times larger than the critical crack half-length L_c . Given that the initiation region itself has to be of the order of L_c and that the abrupt initiation procedure shortens the transition distances (as we show in the following sections), the case with $f_d = 0.2$ corresponds to supershear transition being close to the initiation site in comparison with the critical crack size. We study both this case (Section 3), as well as the case with a different seismic ratio $s = 1.0$ ($f_d = 0.34$), which results, according

to eq. (1), in transition distances much larger than the critical crack size, $L/L_c = 21.5$ (Section 4).

Hence the two primary goals of this work are to study supershear transition with a dynamic initiation procedure that mimics the experiments and to consider two different parameter regimes that result in significantly different ratios of transition distances and critical crack sizes. These goals are closely related. One would expect the initiation procedure to have a different effect on the length and mode of supershear transition, depending on how close the location of the transition is to the rupture initiation region. This expectation is supported by our study, as described in Sections 3 and 4. Indeed, even the mechanism of the supershear transition is different in the two-parameter regimes, for cases that match experimentally determined transition distances. Comparisons between the two regimes and conclusions are given in Sections 5 and 6.

2 MODEL FOR SIMULATING SUPERSHEAR TRANSITION

Our model (Fig. 1) is based on the configuration used by Xia *et al.* (2004). We consider a planar interface in a thin Homalite plate, in the context of a 2-D plane-stress problem. Homalite has the following material properties (Dally & Riley 1991): Young's modulus $E = 3860$ MPa, shear modulus $\mu = 1429.63$ MPa, Poisson's ratio $\nu = 0.35$, density $\rho = 1200$ kg m $^{-3}$, and shear wave speed $c_s = 1078.10$ m s $^{-1}$. The interface is pre-stressed with shear and normal stresses $\tau_0 = P \sin \alpha \cos \alpha$ and $\sigma_0 = P \cos^2 \alpha$, respectively, with the non-dimensional pre-stress $\tau_0/\sigma_0 = \tan \alpha$ being independent of P . Following Xia *et al.* (2004), we set $\alpha = 25^\circ$ and use several values of P , ranging from 8 to 16 MPa. As in the study of Andrews (1976), the interface friction is modelled as linear slip-weakening friction. The static friction coefficient for the experimental interfaces is well constrained as $f_s = 0.6$ (Xia *et al.* 2004), a typical value for many materials including rocks.

The values of the dynamic friction coefficient f_d and critical slip D_c are less certain, and we study two values of f_d and several options for D_c . Xia *et al.* (2004) used $f_d = 0.2$ and, based on the analysis of the experiments using the results of Andrews (1976), determined that $D_c = 10$ μ m for $P = 9$ MPa. As described in detail by Rosakis *et al.* (2007), the best fit to experiments was achieved with a pressure-dependent D_c derived based on experiments by Ohnaka (2003) and a micromechanical model:

$$D_c = c[(\tau_s - \tau_d)/\tau_d]^M \sqrt{H} a_0 \cos \alpha \cdot P^{-1/2} \propto P^{-1/2}, \quad (4)$$

where c and M are experimentally determined constants, H is the hardness of the material, and a_0 is the average radius of contacting asperities (which is assumed constant). Substituting (4) into (2), one finds that the transition length L is then proportional to $P^{-3/2}$ as follows:

$$L = F(s) \frac{\mu(f_s - f_d)}{\pi(1 - \nu)(\sin \alpha - f_d \cos \alpha)^2} c \left(\frac{f_s - f_d}{f_d} \right)^M \times \sqrt{H} a_0 \cos \alpha \cdot P^{-3/2} \propto P^{-3/2}. \quad (5)$$

In the cases where we consider effects of the pressure-dependent D_c , we set the value of $D_c = D_c^{\text{ref}}$ for one value of the external compression $P = P^{\text{ref}}$, and assign the rest of the values according to $D_c = D_c^{\text{ref}} (P/P^{\text{ref}})^{-1/2}$. In Section 3, we use the set of values proposed by Xia *et al.* (2004), with $f_d = 0.2$ and $s = 0.5$. However, the value $f_d = 0.2$ has been determined only approximately, as discussed in Section 1. In Section 4, we consider cases with the different seismic ratio of $s = 1.0$, corresponding to $f_d = 0.34$. Since the ratio of the transition distance L to the critical crack half-size L_c is almost

an order of magnitude larger in the second parameter regime as discussed in Section 1, we use an order of magnitude smaller value of D_c (and hence L_c) in Section 4, so that the predicted un-normalized lengths of the transition distance still matches the experimental measurements with a drastically different set of parameters. We consider both pressure-independent and pressure-dependent D_c in Sections 3 and 4.

The numerical simulations in this work are performed using a spectral boundary-integral method (Geubelle & Rice 1995; Liu & Lapusta 2008). The elastodynamic response of the surrounding medium is expressed as an integral relationship between the stress and slip on the interface, in the form:

$$\tau(x, t) = \tau_l(x, t) + \varphi(x, t) - \frac{\mu}{2c_s} \dot{\delta}(x, t), \quad (6)$$

where $\tau(x, t)$ is the shear stress on the interface, $\tau_l(x, t)$ is the shear stress that would act on the interface in the absence of slip, $\varphi(x, t)$ is the functional of slip history on the interface and $\dot{\delta}(x, t)$ is the slip (or sliding) velocity. The functional $\varphi(x, t)$ is related to slip history in the Fourier domain. This means that the simulated spatial domain is periodically replicated along the interface. The spatial domain in the simulations is chosen to be large enough to ensure that no waves arrive from replicated rupture processes within the time window of interest. This is consistent with the experimental approach in which supershear transition and propagation were observed for times short enough that no wave reflections could have arrived from the sample boundaries (Rosakis *et al.* 2007). We use the numerical implementation of Liu & Lapusta (2008). In our model, the interface is discretized uniformly with such a grid that the ratio of the critical crack half-length L_c and cell size h ranges from 50 to 500 for different parameter selections. In a number of cases, twice better resolution has been used to verify the numerical convergence. In all such cases, the results are virtually indistinguishable between the two resolutions; for example, the difference in the peak slip velocity is less than 1 per cent. The cohesive zone size is well resolved in all simulations.

Our procedure of the rupture initiation (Fig. 1) is intended to capture the dynamic nature of the wire explosion described in Section 1. While the wire is less than 0.1 mm thick, it turns into plasma due to the electric current surge, and hence it can affect a larger region along the interface than the 0.1-mm thickness would suggest. After each experiment, the interface surfaces contain a thin layer of metallic particles around the explosion site. The spatial extent of the layer is typically 4–10 mm along the interface. We model the effect of the plasma by applying a reduction $\Delta\sigma$ of normal stress over a region of size $2a$. For simplicity, we keep the normal stress reduction uniform over that region. In most of our simulations, the duration of the normal-stress reduction is $T_0 = 5 \mu\text{s}$, consistently with estimates of Rosakis *et al.* (2007). Normal stress is reduced by $\Delta\sigma$ linearly over $1 \mu\text{s}$, kept at the level $(\sigma_0 - \Delta\sigma)$ for $3 \mu\text{s}$, and then brought back to the original level linearly over $1 \mu\text{s}$ (Fig. 1). We explore the consequences of varying the duration T_0 of the normal-stress reduction in Sections 3.4 and 4.4. The normal-stress variation reduces the frictional strength of the interface and allows the sliding to initiate and develop under the applied shear stress. Note that the normal-stress reduction $\Delta\sigma$ used is always smaller than the applied normal stress σ_0 so that there is no interface opening. In the experiments, the wire explosion might cause local opening of the interface; investigating such scenarios is a goal for future research. As discussed in Section 1, our representation of the initiation procedure allows us to explore two aspects that were not a part of the original analysis by Andrews (1976): the dynamic and transient na-

ture of the initiation procedure and the fact that, in the experiments, the initiation procedure is independent of the far-field pressure P .

Our aim is to determine the suite of potential transition scenarios relevant to the experimental set up of Xia *et al.* (2004). To that end, for each set of friction properties that we study, we consider a range of values for parameters a and $\Delta\sigma$ and choose the ones that give us the best match to experimental observations. This approach not only allows us to determine the range of potential rupture behaviours consistent with the experimental measurements but also outlines the space of plausible initiation parameters, which would be helpful in our future work on quantifying the explosion. Once a set of friction properties has been specified, the choice of rupture initiation parameters becomes relatively restricted by the fact that the same initiation procedure has to initiate spontaneous rupture propagation for all P of interest, from 8 to 16 MPa. The range of P implies a range in the values of the critical crack half-size L_c , and it is likely that, for successful rupture initiation, the half-size a of the initiation region should be comparable to L_c for all P of interest, with the parameter a/L_c being comparable to 1. In addition, the normal stress change $\Delta\sigma$ should be large enough to initiate sliding for all values of P , which means that the condition $(\sigma_0 - \Delta\sigma)f_s < \tau_0$ should be satisfied for all P . This condition is the most restrictive for the largest value of P and, for $\alpha = 25^\circ$ and P from 8 to 16 MPa, translates into the requirement $\Delta\sigma \geq 2.9$ MPa. Since we consider here cases with no opening, we also require that $\Delta\sigma < \sigma_0$ for all P , which results in $\Delta\sigma < 6.6$ MPa.

How do the different initiation parameters affect the rupture nucleation and evolution? Clearly, the larger the parameter a/L_c , the better are the conditions for the initiation of spontaneous rupture. Since larger values of P correspond to smaller values of L_c , a constant value of a would result in the parameter a/L_c being larger for larger P , and hence more favourable for initiation. The effect of the normal stress decrease $\Delta\sigma$ can be measured by the initial slip velocity $\dot{\delta}_{\text{ini}}$ that such decrease would cause if it happened instantaneously. That slip velocity can be computed from the elastodynamic relation (6). After an abrupt stress drop, we have, in the beginning of sliding, $\varphi = 0$, $\tau_l = \tau_0$, $\tau = (\sigma_0 - \Delta\sigma)f_s$, and

$$\dot{\delta}_{\text{ini}} = \frac{2c_s}{\mu} (f_s \Delta\sigma + \tau_0 - f_s \sigma_0) = \frac{2c_s}{\mu} (0.6\Delta\sigma - 0.1P). \quad (7)$$

Hence the larger $\Delta\sigma$ is, the larger the slip velocity, which would be induced. However, the slip velocity also depends on P , with larger values for smaller P . For example, an abrupt drop of $\Delta\sigma = 5$ MPa would induce slip velocity of 3.3 m s^{-1} for $P = 8$ MPa and 2.7 m s^{-1} for $P = 12$ MPa. Hence a particular value of $\Delta\sigma$ would favour rupture development for smaller values of P . In the initiation procedure in our model, we apply the stress drop over the time of $1 \mu\text{s}$, so the effect would be more complex than estimated here, however the above calculation gives an order-of-magnitude estimate. Finally, the duration of the rupture initiation procedure is important, since, after the normal stress is again increased to the initial value in the region of the nucleation procedure, the slip velocities would be reduced in that region. That should have a varying effect on the rupture development, depending on how large the rupture is at that point. The length of the rupture would depend on how the rupture speed evolves. To get an order-of-magnitude estimate, let us assume that the rupture velocity would be close to c_R , so that in time T_0 the rupture would advance by about $c_R T_0$. Then $(c_R T_0 + a)/a$ would give an estimate of how much larger the rupture is than the region affected by the reduced slip velocities, whereas $c_R T_0/L_c$ would indicate how much beyond the initiation region the rupture has had the chance to propagate before the normal

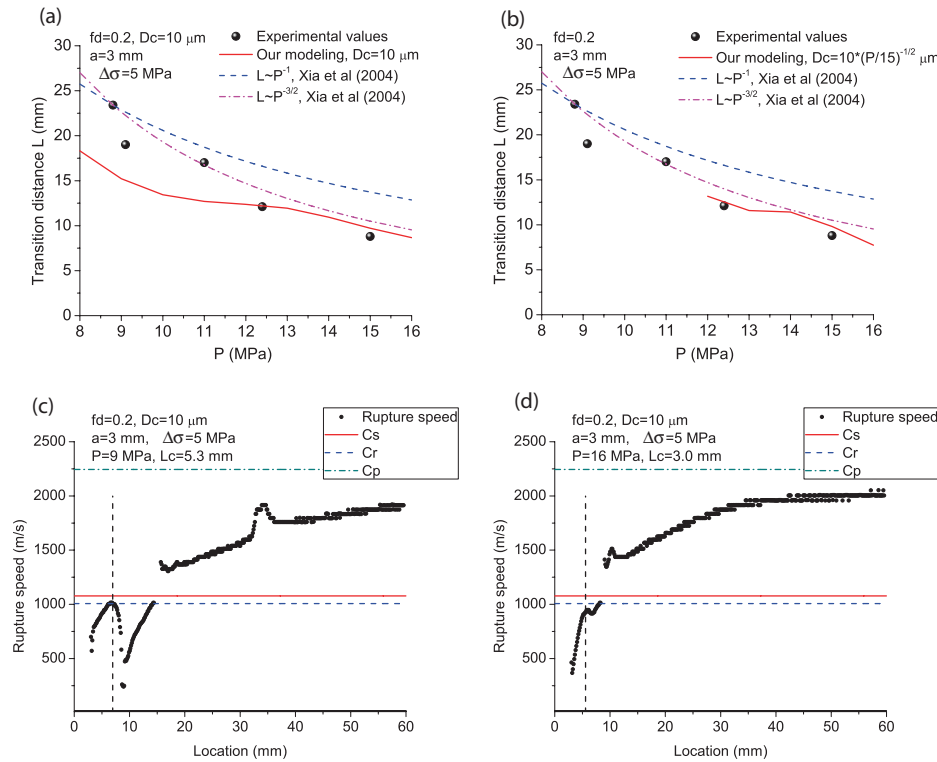


Figure 2. Simulation results for $f_d = 0.2$, $\Delta\sigma = 5$ MPa, $a = 3$ mm and $T_0 = 5$ μ s. (a) The dependence of supershear transition distances L on the compression P obtained in our simulations with pressure-independent $D_c = 10$ μ m (the solid red curve). The experimental results (dots), the results with pressure-independent $D_c = 10$ μ m (and hence $L \sim P^{-1}$) from Xia *et al.* (2004) (the blue dashed curve), and the results with pressure-dependent $D_c \propto P^{-1/2}$ ($L \sim P^{-3/2}$) from Xia *et al.* (2004) (the violet double-dashed curve) are given for comparison. (b) An attempt to better fit experimental results in our simulations by incorporating pressure-dependent $D_c \propto P^{-1/2}$ with $D_c = 10$ μ m for $P = 15$ MPa (the solid red curve). In this case, rupture arrests for $P < 12$ MPa. (c) and (d) Rupture speed versus the location of the rupture tip for the cases of $P = 9$ MPa (panel c) and $P = 16$ MPa (panel d), with the pressure-independent $D_c = 10$ μ m. The supershear transition distances plotted in Fig. 2(a) correspond to the location of the crack tip when the speed transition occurs ($L = 15$ mm for $P = 9$ MPa and $L = 8$ mm for $P = 16$ MPa). The vertical dashed line corresponds to the rupture tip position at end of the initiation process, when $t = T_0 = 5$ μ s. For $P = 9$ MPa, there is a prominent slow-down in the rupture speed due to the end of the normal stress reduction in the rupture initiation region. For $P = 16$ MPa, the rupture speed is reduced much less.

stress reduction effect disappears, with respect to the critical half-size L_c .

In this work, we use the critical crack half-size L_c as the reference spatial scale for rupture propagation. Uenishi & Rice (2003) studied the initiation of a frictional shear crack subjected to peaked quasi-static loading with slips that do not exceed D_c . They demonstrated that the crack would become dynamic when its half length reaches the critical value

$$L_{\text{nucl}} = \frac{0.579\mu D_c}{(1-\nu)(\tau_s - \tau_d)}. \quad (8)$$

Neither parameter L_c nor parameter L_{nucl} are directly relevant to the initiation procedure in this study, since the procedure involves inertial effects while both parameters are based on quasi-static considerations. We use L_c as the reference length to enable easy comparison with previous studies. Note that the ratio

$$L_{\text{nucl}}/L_c = 0.579\pi \frac{(\tau_0 - \tau_d)^2}{(\tau_s - \tau_d)^2} = 0.579\pi \frac{1}{(1+s)^2} \quad (9)$$

does not depend on the compression P . For $s = 0.5$ and 1.0, $L_{\text{nucl}}/L_c = 0.81$ and 0.43, respectively. Hence we see that the two parameters are comparable for the cases we consider in this work.

3 SIMULATIONS OF SUPERSHEAR TRANSITION FOR THE SEISMIC RATIO $s = 0.5$ ($f_d = 0.2$)

We start by exploring the case proposed by Xia *et al.* (2004) of $s = 0.5$, $f_d = 0.2$ and $L/L_c = 4.8$ based on eq. (1). As discussed in the following, the ratio of L/L_c becomes even smaller in our simulations due to the dynamic rupture initiation procedure. We refer to this parameter regime as the one in which the transition occurs close to the initiation region, in non-dimensional terms.

3.1 Comparison of experimental and simulated transition distances for the parameters of Xia *et al.* (2004)

Fig. 2(a) shows the experimentally measured transition distances (shown as dots); they vary from about $L = 20$ mm for $P = 9$ MPa to about $L = 10$ mm for $P = 15$ MPa. The exact values are given in Table 1. To compare these results with the work of Andrews (1976),

Table 1. Experimentally measured supershear transition distances L for different P (Xia *et al.* 2004; Rosakis *et al.* 2007).

P (MPa)	8.8	9.1	11.0	12.4	15.0
L (mm)	23.4	19.0	17.0	12.1	8.8

Xia *et al.* (2004) and Rosakis *et al.* (2007) matched the observed and theoretical transition distances for the first experimental data point of Fig. 2(a) ($P = 8.8$ MPa, $L = 23.4$ mm), inferring $L_c = 5.5$ mm and $D_c = 10$ μm . By assuming the pressure-independent value of $D_c = 10$ μm and pressure-dependent values of D_c given by eq. (4), they used eqs. (2) and (5), respectively to predict the dependence of the transition length on P as shown in Fig. 2(a). These curves are marked as $L \sim P^{-1}$ and $L \sim P^{-3/2}$, respectively. Clearly, the pressure-dependent D_c gives a better match.

The red solid line in Fig. 2(a) shows the transition distances obtained through the current simulations with pressure-independent $D_c = 10$ μm and rupture initiation parameters $a = 3$ mm and $\Delta\sigma = 5$ MPa. Note that this selection of a is consistent with the size of the region covered by the wire debris particles discussed in Section 2. As P varies from 8 to 16 MPa, L_c varies from 6 to 3 mm, and a/L_c varies from 0.5 to 1.0. In comparison to the results (2) of Xia *et al.* (2004), the simulated transition distances in our model are 30–40 per cent smaller, indicating that the dynamic rupture initiation mechanism indeed acts to shorten the transition distance. The ratio of the numerically simulated L to L_c is only about 3 on average. The overall trend with P is similar between the predictions (2) and our simulations. The simulated values do not fit the experimental results (shown as dots), underestimating transition distances for lower values of compression P . We have studied a number of different parameters for the rupture initiation procedure, and it seems impossible to make the simulations agree with the experimental values for $D_c = 10$ μm . In particular, as parameters a and/or $\Delta\sigma$ are decreased, the simulated transition distances for lower values of P remain too short until the initiation procedure fails to initiate ruptures for these lower values of P .

Would incorporating the pressure-dependent D_c help to match the transition distances better? Keeping the same $D_c = 10$ μm for $P = 9$ MPa and decreasing D_c for larger values of P , as done in Xia *et al.* (2004), clearly would not work, as this would simply retain the shorter transition distances for lower P and shorten the transition distances for higher P , making the overall comparison with experimental results even worse. We have confirmed this conclusion in our simulations. However, we can keep the value of $D_c = 10$ μm for $P = 15$ MPa and increase the value of D_c for smaller values of P in accordance with (5). Theoretically, this should produce the desired effect, as larger values of D_c translate into larger values of L_c and, for the same seismic ratio, potentially result in larger values of the transition distance L . However, simulations for this case show that the initiation procedure fails to start a spontaneous crack for $P < 12$ MPa. The results, in terms of supershear transition distances, are shown in Fig. 2(b) (red solid curve). For $P < 12$ MPa, the rupture does not propagate, and hence it does not transition to supershear speeds.

The rupture fails to initiate for smaller values of P because such values result in larger critical crack half-sizes L_c (everything else being equal), which has two effects on the rupture initiation. First, the ratio a/D_c decreases, so that the normal stress reduction affects a smaller portion of the critical crack size. Second, in the time T_0 that the normal stress reduction lasts ($T_0 = 5$ μs here), the rupture tends to acquire a smaller length in terms of L_c , and hence the rupture may be less developed when the normal stress goes back to its original value and increases the resistance to sliding over a part of the rupture. This effect is discussed further in Section 3.2. Note that $c_R T_0/L_c$, the related parameter discussed in Section 2, varies from 0.6 to 1.7 as P varies from 8 to 16 MPa, illustrating why the rupture would be affected by the end of the rupture initiation procedure for all values of P but especially for smaller P .

3.2 Rupture evolution and direct supershear transition at the rupture tip

The typical simulated rupture evolution is illustrated in Figs 2(c) and (d) where the rupture speed is plotted for two cases from Fig. 2(a), $P = 9$ MPa and $P = 16$ MPa, both with $D_c = 10$ μm . For both cases, the rupture accelerates and approaches the Rayleigh wave speed c_R during the normal-stress reduction in the nucleation region. However, when the normal stress goes back to the original level in the nucleation region (vertical dashed lines in Figs 2c and d), the frictional resistance increases relatively abruptly in the nucleation region causing decrease in slip velocities. When the information about that decrease arrives at the rupture tip, the rupture speed decreases. The decrease in rupture speed is more substantial for the case of $P = 9$ MPa and only slight for the case of $P = 16$ MPa, consistently with our discussion of the differences between lower and higher values of P at the end of Section 3.1. The critical crack half-sizes L_c are 5.3 and 3.0 mm for 9 and 16 MPa, respectively. Figs 2(c) and (d) show that, at the time of the rupture speed decrease that signifies the end of the normal stress reduction in the initiation region, the rupture lengths are 6.9 mm = $1.3L_c$ for $P = 9$ MPa and 5.6 mm = $1.9L_c$ for $P = 16$ MPa. Hence, at the end of the initiation procedure, the rupture is less developed, in terms of L_c , for $P = 9$ MPa than for $P = 16$ MPa. (This distinction is qualitatively captured by the parameter $c_R T_0/L_c$ discussed in Section 2, which is equal to 0.9 for $P = 9$ MPa and 1.7 for $P = 16$ MPa, indicating that the crack is likely to be less developed for $P = 9$ MPa.) That is why the rupture slows down much more for the case of $P = 9$ MPa. In both cases, the rupture recovers and transitions to supershear speeds soon after.

To illustrate how the transition takes place, we plot, in Fig. 3, two snapshots of the slip velocity and shear stress distribution, one before the transition and one after, for the case of $P = 9$ MPa, $D_c = 10$ μm . The values of shear stress normalized by the normal stress σ_0 are shown, with 0.6 corresponding to the static friction coefficient. At the time $t = 16$ μs (Fig. 3a), the rupture tip is at the location of $x = 14.2$ mm ($x = 0$ corresponds to the middle of the initiation region and hence the middle of the rupture), and the region $0 \leq x \leq 14.2$ mm represents half of the current rupture extent. The normalized shear stress at the location of the rupture tip is 0.6, as appropriate for the point that has just reached the static friction threshold. The shear stress peak at $x = 20$ mm is a classical feature of mode II ruptures described in the work of Burridge (1973) and Andrews (1976). That peak travels with the shear wave speed and represents a pile-up of stress due to shear waves. If the peak reaches the static friction level, a supershear daughter crack would nucleate there, resulting in the Burridge–Andrews transition mechanism. At the time $t = 16$ μs , the shear stress peak is below the static friction level; Fig. 2(c) shows that, when the crack tip is at the location of 14.2 mm, the rupture is still sub-Rayleigh. At $t = 20$ μs , not much has changed in the shape of the shear stress, which simply advanced along the interface. However, the rupture front is now at $x = 19.3$ mm, and Fig. 2(c) indicates that the rupture is supershear at this point. Clearly, there is no separate daughter crack, at the shear stress peak or otherwise; rather, we see a perturbation in slip velocities right at the rupture tip, indicating that the crack front itself is transitioning to supershear speeds. This direct transition at the rupture tip has been studied in the works of Geubelle & Kubair (2001), Dunham (2007) and Liu & Lapusta (2008).

Hence we find that supershear transition in this parameter regime occurs by the direct change of rupture speed at the rupture tip, and not by the Burridge–Andrews mechanism. There is an easy

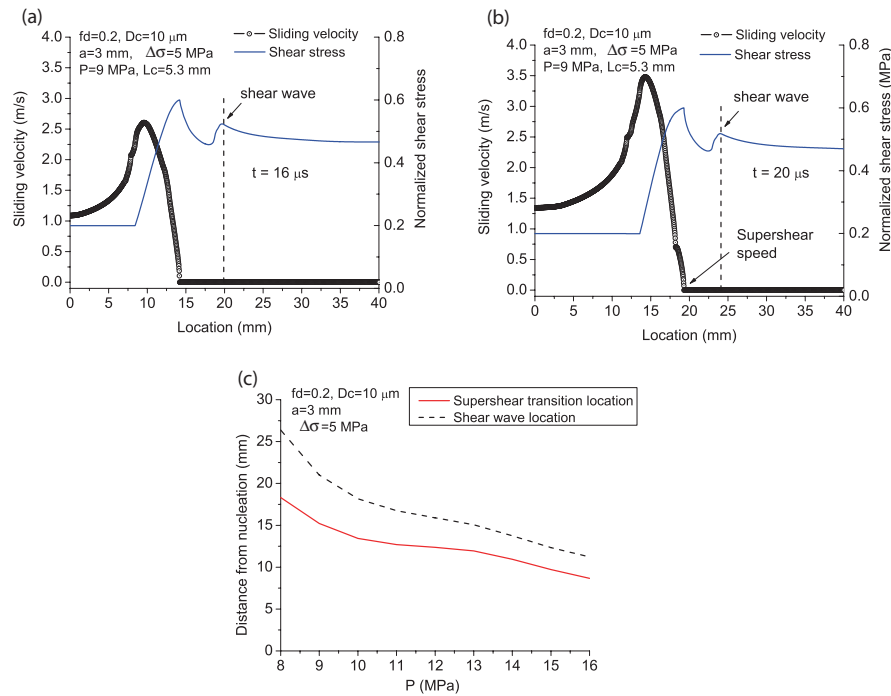


Figure 3. Direct supershear transition at the rupture tip. (a) and (b) Snapshots of sliding velocity and normalized shear stress before and after supershear transition for the simulation of Fig. 2(c). The shear stress peak travelling with the shear wave speed in front of the main rupture has not yet reached the static friction strength and no daughter crack is initiated. Instead, supershear transition occurs right at the rupture tip as its speed directly jumps from the Rayleigh wave speed to a supershear speed. The vertical dashed lines indicate the first arrival of the shear wave, which is computed from the edge of the nucleation region. (c) Locations of the shear wave front and rupture tip when supershear transition occurs for the case of Fig. 2(a). We see that, for all P , the location of supershear transition is behind the shear wave peak.

way to check the transition mechanism for other values of P . For the case of Figs 3(a) and (b), the actual transition distance is $L = 15.2$ mm. Note that the shear stress peak is ahead by about 5 mm in both snapshots, which means that the shear stress peak was at about $x = 20$ mm at the time of the transition. To check whether the transition occurs at the shear stress peak, one can simply plot the transition distance and the location of the shear stress peak at the time of the transition and see whether they coincide. This is done in Fig. 3(c), which demonstrates that the shear stress peak is clearly ahead of the supershear transition location for all values of P , indicating that supershear transition occurs not by the Burridge–Andrews (mother–daughter) mechanism but rather by the direct transition at the rupture tip.

3.3 Set of parameters that fits experimental data

Section 3.1 considers supershear transition distances obtained with the values of D_c inferred by Xia *et al.* (2004). The simulated transition distances with $D_c = 10 \mu\text{m}$ are mostly smaller than the experimental values (Fig. 2a), especially for lower values of compression P . Based on those results, we have conducted a series of simulations with larger D_c aiming to increase L_c and hence the transition distances L , assuming that L/L_c stays approximately the same. Fig. 4(a) shows the results for $D_c = 13 \mu\text{m}$ and $a = 5$ mm. Overall, the transition distances are matched better than for $D_c = 10 \mu\text{m}$, but discrepancies remain. In particular, the dependence of the simulated transition distances on P is segmented into two parts separated by $P = 12$ MPa. Note that, as P varies from 8 to 16 MPa, L_c varies from 7.8 to 3.9 mm, a/L_c varies from 0.64 to 1.28, and the ratio of a/L_c acquires the value of 1 at approximately $P = 12$ MPa. This means that the rupture initiation procedure is the likely cause of

the segmentation, and in particular the rupture slow-down it causes as normal stress returns to the original value in the rupture initiation region. Similarly to the discussion in Section 3.2, the rupture is not yet well developed in terms of L_c for $P < 12$ MPa at the end of the normal stress perturbation, and that is why the rupture slow-down is more pronounced for lower P . That results in longer rupture recovery from the slow-down, and hence in larger transition distances than the rupture would have had without the slow-down (Fig. 4c). For $P \geq 12$ MPa, the slow down is much smaller and approximately the same for all P (Fig. 4d), resulting in transition distances decreasing with P in a manner more similar to, if slightly faster than, the results of Xia *et al.* (2004).

In Fig. 4(b), we plot the transition distances L simulated with pressure-dependent $D_c \propto P^{-1/2}$, with $D_c = 13 \mu\text{m}$ for $P = 9$ MPa. The dependence of L on P is still separated into two trends, similarly to the case of Fig. 4(a). For the pressure-dependent D_c , L_c decreases faster with P than for the case with the constant, pressure-independent D_c of Fig. 4(a), and hence the separating point of the two trends on the transition curve moves from 12 to 10 MPa. The overall agreement of the simulated and experimental values of L is somewhat worse for the pressure-dependent D_c than for the constant one (Figs 4(b) versus Fig. 4(a), although it is possible that small adjustments in the parameters of the rupture initiation procedure would result in a better fit.

3.4 Dependence of supershear transition on parameters of the rupture initiation procedure

In Section 3.3, we used the following parameters of the rupture initiation procedure: $a = 5$ mm (with a/L_c varying from 0.64 to 1.28 for the range of P considered), $\Delta\sigma = 5$ MPa, and

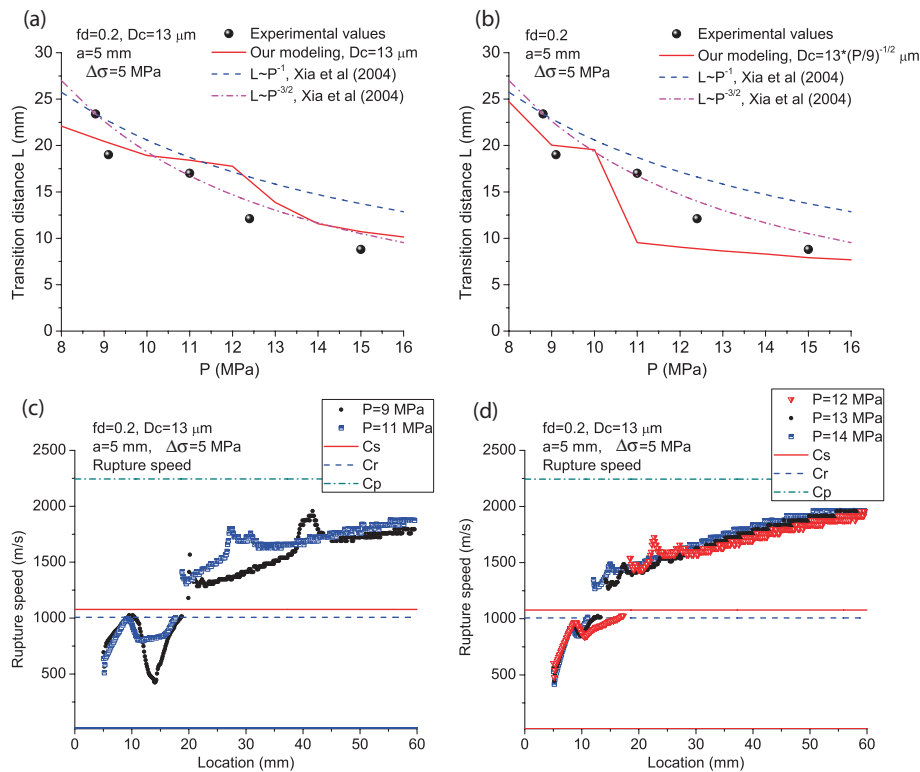


Figure 4. Simulation results for $f_d = 0.2$ with a set of parameters that provides a better fit to experimental transition distances. (a) and (b) The dependence of the simulated supershear transition distances L on the compression P (solid red curve) for $D_c = 13 \mu\text{m}$ (panel a) and $D_c \propto P^{-1/2}$ with $D_c = 13 \mu\text{m}$ for $P = 9 \text{ MPa}$ (panel b), with $a = 5 \text{ mm}$, $\Delta\sigma = 5 \text{ MPa}$, and $T_0 = 5 \mu\text{s}$. The overall fit is improved in comparison to Figs 2(a) and (b); the segmentation of the simulated curves is discussed in the text. The results of Xia *et al.* (2004) are shown for the same parameters as in Fig. 2(a), for comparison. (c) and (d) Rupture speed versus the location of the rupture tip in the case of pressure-independent $D_c = 13 \mu\text{m}$ (Fig. 4a) for $P = 9, 11 \text{ MPa}$ (panel c) and $P = 12, 13$ and 14 MPa (panel d). The rupture speed experiences a longer slow-down for the smaller values of P , which is the likely cause of the curve segmentation of Fig. 4(a).

$T_0 = 5 \mu\text{s}$. Fig. 5 shows how supershear transition distances are affected when these parameters are varied. Overall, the behaviour is not a simple translational change. For example, one might expect that larger values a of the size of the initiation zone would create a larger initial crack, enhance the rupture acceleration, and hence shorten transition distances. However, this expectation is not supported by simulations for some combinations of a and P (Fig. 5a). This is because the crack evolution history is quite complex and differs for different values of P , as discussed in Sections 3.2 and 3.3, and there are competing effects. One competing effect is that a larger value of a means that a larger part of the expanding rupture will be affected by the end of the initiation procedure, causing a larger slow-down in the rupture speed and delaying the supershear transition. For different values of P , different competing effects win, resulting in complex dependencies shown in Fig. 5. Similar considerations apply to results for different values of the stress drop $\Delta\sigma$ and explosion duration T_0 . Note that all simulations are well-resolved numerically.

The results shown in Fig. 5 indicate that, for this parameter regime of direct transition at the rupture tip with relatively small L/L_c , the transition distances cannot be made much larger than what we see in Fig. 5. If we use a weaker initiation procedure, with smaller values of a , $\Delta\sigma$ or T_0 , then the rupture would fail to initiate for some values of P ; we already see that effect, for smaller values of P , in Fig. 5(a) for $a = 4 \text{ mm}$ and in Fig. 5(c) for $T_0 = 4 \mu\text{s}$. That is why, after establishing that the transition distances are too short for the case of $D_c = 10 \mu\text{m}$ in Sections 3.1 and 3.2, we could not increase those transition distances simply by varying parameters of

the initiation procedure. As a side note, the transition distance L is larger than a by definition, as the location of the crack tip starts at $x = a$ and L is defined as the distance between the middle of the initiation zone ($x = 0$) and the rupture tip when the rupture first acquires supershear speeds. Hence the values of transition distances cannot be smaller than a .

Some parameters of the initiation procedure lead to ruptures that experience two transitions to supershear speeds. This is illustrated in Fig. 6. The first transition, with the rupture tip at about 10 mm , occurs right when the rupture initiation procedure stops (Fig. 6a). It takes some time for the rupture front to receive that information through radiated waves, and the resulting slow-down of the rupture makes the rupture transition back to sub-Rayleigh speeds. The rupture recovers and transitions to sustained supershear speeds later, at the location of about 22 mm . In the corresponding plots of the transition distances versus P , we plot both of the transition attempts, which results in two branches for dashed blue curves (Figs 6b and 5). The example of Fig. 6(a) is marked in Fig. 6(b) by a blue solid circle (for a failed transition attempt) and a blue solid square (for the sustained supershear transition). This behaviour helps explain the non-monotonic variation of the transition distances with the rupture initiation parameters evident in Fig. 5.

3.5 Dominance of the direct supershear transition for the seismic ratio $s = 0.5$ ($f_d = 0.2$)

In all the cases presented in Sections 3.1–3.4, the transition occurs directly at the rupture front before the mother–daughter crack

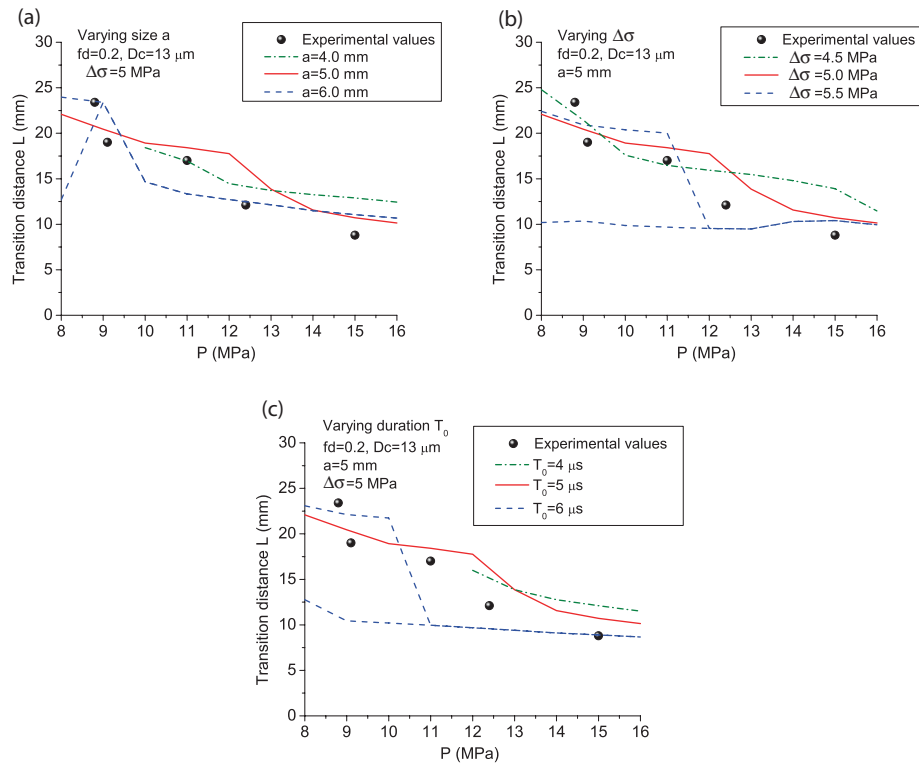


Figure 5. Dependence of transition distances on the parameters of the initiation procedure for the case of $f_d = 0.2$ and pressure-independent $D_c = 13 \mu\text{m}$. The reference set of the rupture initiation parameters is that of Fig. 4(a), $a = 5 \text{ mm}$, $\Delta\sigma = 5 \text{ MPa}$, and $T_0 = 5 \mu\text{s}$. In each panel, one of these parameters is varied and the results are shown for simulations with different values of: (a) the half-size a of the rupture initiation procedure, (b) normal stress reduction $\Delta\sigma$ and (c) duration T_0 . In each panel, the blue dashed line gives transition distances for the largest value of the parameter studied, and that line has two branches for lower values of P . The two branches correspond to a failed attempt to transition and then to the actual sustained transition to supershear speeds, as illustrated in Fig. 6.

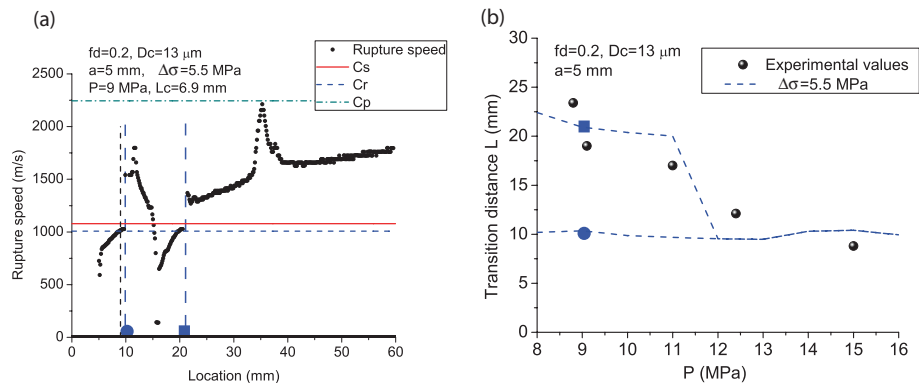


Figure 6. A representative case with two supershear transition stages, for $f_d = 0.2$, $D_c = 13 \mu\text{m}$, $a = 5 \text{ mm}$, $\Delta\sigma = 5.5 \text{ MPa}$ and $T_0 = 5 \mu\text{s}$. (a) Rupture speed versus the location of the rupture tip for $P = 9 \text{ MPa}$. The failed and successful attempt of supershear transition are marked by a solid blue circle and square, respectively, and blue dotted lines. (b) The dependence of transition distances on P . Plotting both the failed and the successful attempt results in two branches for lower values of P .

mechanism has a chance to act. We discuss the possible reasons for this dominance in Section 5, where we compare these cases to the ones of Section 4. The direct transition mechanism is likely caused by waves radiated from the relatively abrupt initiation procedure. The stress field carried by the waves allows the rupture front to meet the static friction threshold with supershear speeds, causing the direct transition. [In fact, as mentioned in Liu & Lapusta (2008), if the initiation procedure is sufficiently strong, the crack can start with supershear speeds right away.] That is why it is not surprising that the timing and location of the supershear

transition for this mechanism are very sensitive to the parameters of the rupture initiation procedure, resulting in non-trivial dependencies discussed in Section 3.4. For this transition mechanism, the transition distances L/L_c should always be relatively short, in the range of 1–3 as observed in Sections 3.1–3.4. This is because the stressing field of the initiation procedure would pass the rupture tip soon after the rupture initiation, when the rupture is still relatively short, and it is at that point that the stress field can influence the rupture tip to transition (or not) to supershear speeds.

If the parameter regime considered in this section is indeed the relevant one for experiments, then a possibility arises that the transition in experiments also happened as the direct transition at the rupture front, and not through the mother–daughter crack mechanism. This is further discussed in Sections 5 and 6. Note that the experimental measurements have up and down variations with P . One interpretation is that such variations represent experimental variability, hugging what should be a smooth curve similar to the results of Andrews (1976). However, as Figs 2 and 4 demonstrate, the dependence of transition distances on P , for this direct mode of supershear transition, is very sensitive to the details of the rupture initiation procedure and values of D_c , resulting in complex segmented plots of L versus P . Hence it is possible that the variation in experimental results at least partially reflects such complexities.

4 SIMULATIONS OF SUPERSHEAR TRANSITION FOR THE SEISMIC RATIO $s = 1.0$ ($f_d = 0.34$)

In Section 3, the parameter regime $s = 0.5$ ($f_d = 0.2$) is chosen, following Xia *et al.* (2004), which results in small non-dimensional transition distances. To match the experimental results, values of D_c of about $13 \mu\text{m}$ are required. For that parameter regime, the results indicate that the dynamic rupture initiation procedure has a large impact on the supershear transition, not only significantly shortening transition distances but also resulting in the different

transition mechanism, experiencing direct supershear transition of the rupture front.

In this section we explore a different parameter regime with the seismic ratio $s = 1.0$ ($f_d = 0.34$) and much larger non-dimensional transition distances $L/L_c = 21.5$. To match the experimental transition distances, which vary from 10 to 20 mm, we need to have critical crack half sizes of the order of 1 mm, which means that the relevant values of D_c are significantly smaller than in Section 3.

4.1 Good agreement between experimental and simulated transition distances for pressure-independent $D_c = 1 \mu\text{m}$.

The red solid line in Fig. 7(a) shows the transition distances from our simulations in this parameter regime, with pressure-independent $D_c = 1 \mu\text{m}$ and rupture initiation parameters $a = 0.8 \text{ mm}$ and $\Delta\sigma = 3 \text{ MPa}$. Note the good match between the experimental and simulated transition distances. Similarly to Section 3.1, a is chosen so that a/L_c varies from 0.46 to 0.92, as P varies from 8 to 16 MPa and L_c varies from 1.74 to 0.87 mm. The transition distances simulated in our model are 30–50 per cent smaller than the predictions (2) of Xia *et al.* (2004) based on pressure-independent D_c (and hence with $L \sim P^{-1}$). This indicates that the dynamic rupture initiation mechanism acts to shorten the transition distances in this parameter regime as well. However, the ratio of the numerically simulated L to L_c is still quite large, about 12 on average.

The simulated rupture evolution in terms of its rupture speed is shown in Figs 7(b)–(d) for three values of P . In all three cases,

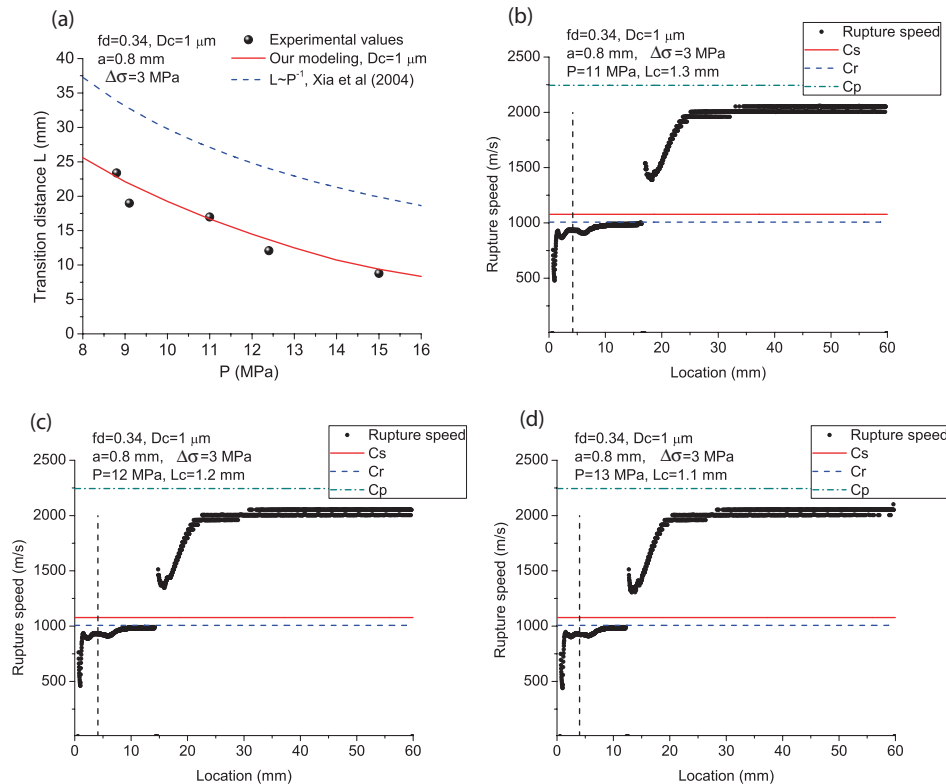


Figure 7. Simulation results for $f_d = 0.34$, pressure-independent $D_c = 1 \mu\text{m}$, $\Delta\sigma = 3 \text{ MPa}$, $a = 0.8 \text{ mm}$ and $T_0 = 5 \mu\text{s}$. (a) The dependence of supershear transition distances L on the compression P in our simulations (the solid red curve). The simulations fit the experimental results (shown as dots) quite well. The transition distances based on the work of Andrews (1976) and the subsequent analysis of Xia *et al.* (2004) with the pressure-independent $D_c = 1 \mu\text{m}$ (and hence $L \sim P^{-1}$) are 30–50 per cent larger (dashed blue curve). Note that the vertical axis has a different range compared to Figs 2(a), 4(a) and 9. (b)–(d) Rupture speed versus the location of the rupture tip for the cases of $P = 11, 12$ and 13 MPa . Vertical dashed lines correspond to the rupture tip position at end of the initiation process, when $t = T_0 = 5 \mu\text{s}$. We see that the effect of the end of the nucleation process on the rupture speed is similar for all P and much smaller than for the cases of Section 3, and that the rupture propagates with speeds close to c_R for a while before transitioning to supershear speeds.

the rupture accelerates and approaches the Rayleigh wave speed c_R during the normal-stress reduction in the nucleation region. Unlike in the cases of Section 3, the rupture speed disruption due to the end of normal-stress reduction is minimal, since, at that point, the rupture is well-developed, with the length of about $3L_c$ to $4L_c$ for different values of P , and the region of normal stress variation constitutes only a small part of the sliding interface. For all three values of P , the rupture propagates with speeds close to c_R for a while before transitioning to supershear speeds. The transition occurs by the Burridge–Andrews (mother–daughter crack) mechanism, as demonstrated in Section 4.2.

The simulated values of the transition distance L decrease faster with P than the predictions (2) of Xia *et al.* (2004) with $L \sim P^{-1}$, which is why the simulated results match the experimental measurements so well, even in this case of pressure-independent D_c . We attribute this faster decrease to the fact that larger values of P correspond to smaller critical crack half-sizes L_c and hence larger ratios of a/L_c . This means that larger P are more affected by the rupture initiation procedure. As discussed in Section 1, that feature was not present in the numerical simulations of Andrews (1976) where the initiation procedure scaled with L_c , and hence it did not enter the subsequent analysis by Xia *et al.* (2004).

4.2 Supershear transition by the Burridge–Andrews (daughter-crack) mechanism

To determine how the supershear transition takes place, we plot, in Fig. 8, two snapshots of the slip velocity and shear stress distribution, one right after the transition and one at a later time, for the case of

$P = 11$ MPa. As in Fig. 3, the values of shear stress normalized by the normal stress σ_0 are shown, with 0.6 corresponding to the static friction coefficient. At the time $t = 17 \mu\text{s}$ (Fig. 8a), the tip of the main rupture is at the location of $x = 15.7$ mm and the region $0 \leq x \leq 15.7$ mm represents half of the current extent of the rupture. The normalized shear stress value at the location of the rupture tip is 0.6. As in Fig. 3, there is a shear stress peak in front of the main rupture, at about $x = 18$ mm, but, unlike in Fig. 3, the shear stress peak is also at 0.6. This has caused the nucleation of a daughter crack at the shear stress peak, which appears on the profile of sliding velocity as a small bump in front of the main rupture. The main rupture and the daughter crack are well separated at this point in time. At $t = 22 \mu\text{s}$ (Fig. 8b), the daughter crack has grown; it is clearly propagating with supershear speeds, as it has overtaken the shear wave front shown by the red dashed line.

Hence we find that supershear transition in this parameter regime occurs by the classical Burridge–Andrews (mother–daughter crack) mechanism. To show that this is the case for all values of P , we plot, in Fig. 8(c), the transition distance and the location of the shear stress peak at the time of the transition. As we can see, they almost coincide for all P , indicating that supershear transition occurs at the shear stress peak, and hence by the mother–daughter crack mechanism.

4.3 Simulations with pressure-dependent D_c

The effect of using pressure-dependent $D_c \propto P^{-1/2}$, with $D_c = 1 \mu\text{m}$ for $P = 9$ MPa, is shown in Fig. 9. In Fig. 9(a), the dashed blue line gives transition distances for the pressure-dependent D_c .

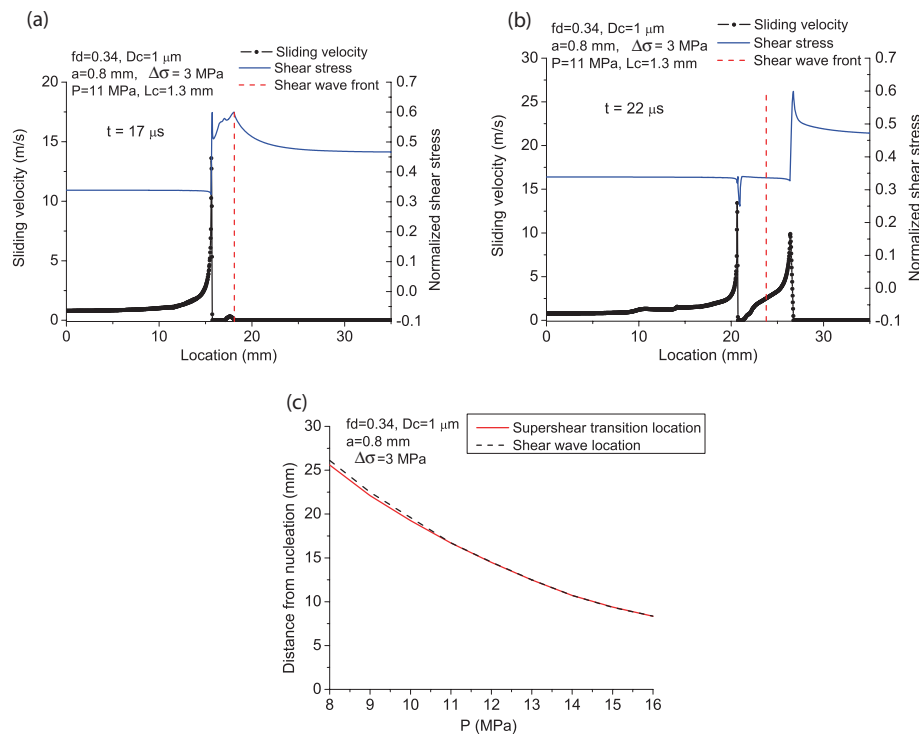


Figure 8. Supershear transition by the Burridge–Andrews mechanism. (a) and (b) Snapshots of sliding velocity and normalized shear stress right after supershear transition and at a later time for the simulation of Fig. 7(b). The shear stress peak travelling with the shear wave speed in front of the main rupture has reached the non-dimensional static friction strength of 0.6 and a daughter crack is initiated (panel a). The daughter crack has supershear speeds and overtakes the shear wave front (panel b). (c) Locations of the shear wave front and rupture tip when supershear transition occurs, for the case of Fig. 7(a). We see that, for all P , the location of supershear transition and the shear stress peak at the shear wave front coincide, indicating transition by the Burridge–Andrews (mother–daughter crack) mechanism in all cases.

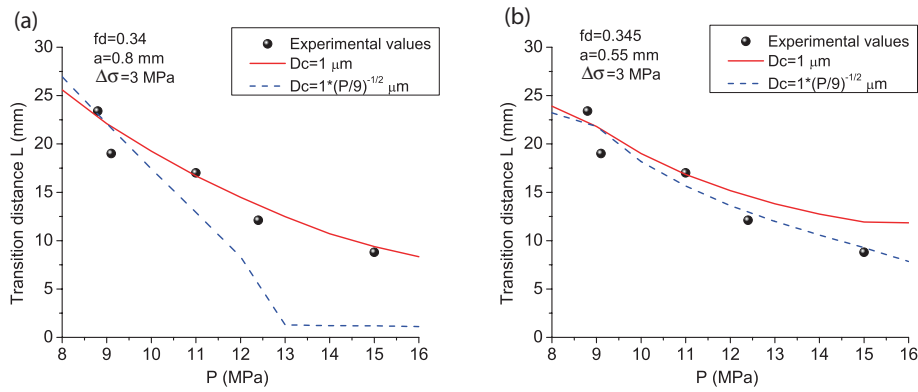


Figure 9. Comparison of supershear transition distances L in simulations with pressure-independent $D_c = 1 \mu\text{m}$ (solid red curves) and pressure-dependent $D_c \propto P^{-1/2}$ with $D_c = 1 \mu\text{m}$ for $P = 9 \text{ MPa}$ (dashed blue curves). (a) Results for parameters of Fig. 7(a), $f_d = 0.34$, $\Delta\sigma = 3 \text{ MPa}$, $a = 0.8 \text{ mm}$ and $T_0 = 5 \mu\text{s}$. Pressure-independent D_c fits the experimental measurements well in this case, while pressure-dependent D_c does not. (b) Results for slightly modified parameters $f_d = 0.345$, $\Delta\sigma = 3 \text{ MPa}$, $a = 0.55 \text{ mm}$ and $T_0 = 5 \mu\text{s}$. In this case, pressure-dependent D_c results in a good match.

We see that the transition distances are too short, falling down rapidly for larger values of P . This is because L_c decreases more rapidly with P in this case, so that a/L_c varies from 0.4 to 1.2 as P varies from 8 to 16 MPa. In fact, the very small transition distances for $P \geq 13 \text{ MPa}$ correspond to the rupture transitioning to supershear speeds directly at its tip right after its initiation, with L/L_c of about 1.5 (this phenomenon is discussed further in Section 4.4). Hence, for this set of parameters, the pressure-dependent D_c does not give a good match to experiments. However, the dynamic friction coefficient and rupture initiation parameters can be slightly adjusted to result in a good fit. For example, selecting $f_d = 0.345$ and $a = 0.55 \text{ mm}$ results in a good match between the experimental results and simulations with pressure-dependent D_c (Fig. 9b, blue dashed curve). Hence the experimental results can be matched well with both pressure-independent and pressure-dependent D_c , with small variations in other parameters.

4.4 Dependence of supershear transition on parameters of the rupture initiation procedure and cases with the direct supershear transition

In Sections 4.1, 4.2 and part of 4.3, we used the following parameters of the rupture initiation procedure: $a = 0.8 \text{ mm}$ (with a/L_c varying from 0.46 to 0.92 for the range of P considered), $\Delta\sigma = 3 \text{ MPa}$, and $T_0 = 5 \mu\text{s}$. Fig. 10 shows how supershear transition distances are affected when these parameters are varied. As in Section 3.4, the overall behaviour is not a simple translational change, although, in this case of larger L/L_c , there is less complexity than in the case of much smaller L/L_c of Section 3.4. In fact, the response of the transition distances L to variations in the duration T_0 (Fig. 10c) is what one would intuitively expect, with larger values of T_0 corresponding to smaller values of L .

For some values of a and $\Delta\sigma$, the transition distances can be much smaller, as the ones we compute for $a = 0.9 \text{ mm}$ and $P \geq 13 \text{ MPa}$ (Fig. 10a), and for $\Delta\sigma = 3.5 \text{ MPa}$ and $P \geq 13 \text{ MPa}$ (Fig. 10b). The origin of such much smaller transition distances is the change in the transition mechanism from the Burridge–Andrews mechanism to the direct transition at the rupture tip. This is illustrated in Fig. 10(a), which shows that the supershear transition for $P = 9 \text{ MPa}$ occurs through the classical mother–daughter crack mechanism, while the supershear transition for $P = 15 \text{ MPa}$ occurs directly at the rupture front. In the latter case, we see that the rupture history is such that no shear stress peak has developed in front of the rupture at the time

of the transition. The normalized transition distances for the direct transition mechanism are small, for example, $L/L_c = 1.7$ for $P = 15 \text{ MPa}$, consistently with our discussion in Section 3.5.

5 DISCUSSION OF THE TWO PARAMETER REGIMES

Our simulations with the rupture initiation procedure that mimics the effects of the wire explosion show that the rupture can transition to supershear speeds by two mechanisms: the direct transition at the rupture tip (Sections 3.2 and 3.5), and the Burridge–Andrews (or mother–daughter crack) mechanism (Section 4.2). Our goal has been to identify parameter combinations which would match all experimentally determined transition distances. After considering cases with two different values of the seismic ratio, $s = 0.5$ (Section 3) and $s = 1.0$ (Section 4), we have found that, in all scenarios with $s = 0.5$ that match experimentally observed values, the transition occurs directly at the crack tip, while in the regime of $s = 1.0$, one can find parameters of the initiation procedure and critical slip D_c that lead to a good match with experimental values for the Burridge–Andrews mechanism.

As discussed in Section 3.5, the direct transition mechanism is likely caused by the relatively abrupt radiation of waves from the rupture initiation procedure. That stress field, when passing by the rupture tip, can enable the tip to meet the static friction threshold with supershear speeds. Note that the nature of typical elastodynamic stress fields is such that stress increases propagate with speeds between the shear wave speed and the dilatational wave speed, and with speeds below the Rayleigh wave speed, while stress decreases propagate with speeds between the Rayleigh wave speed and the shear wave speed. That is why rupture speeds, driven by the elastodynamic stress fields of the problem, are either sub-Rayleigh or supershear. If the relatively abrupt stress field radiated by the rupture initiation passes by the rupture tip without causing the direct transition, then the crack remains sub-Rayleigh until, for sufficiently small seismic ratios s , it develops a large enough shear stress peak in front and transitions to supershear speeds by the mother–daughter crack mechanism.

The parameter regime of Section 3 may favour the direct supershear transition for several reasons. It has lower seismic ratio $s = 0.5$ that promotes supershear transition. It has a higher stress drop, $(\tau_0 - \tau_d)/\sigma_0 = f_0 - f_d$. Another difference between the two parameter regimes is the values of the parameter $c_R T_0/L_c$ which

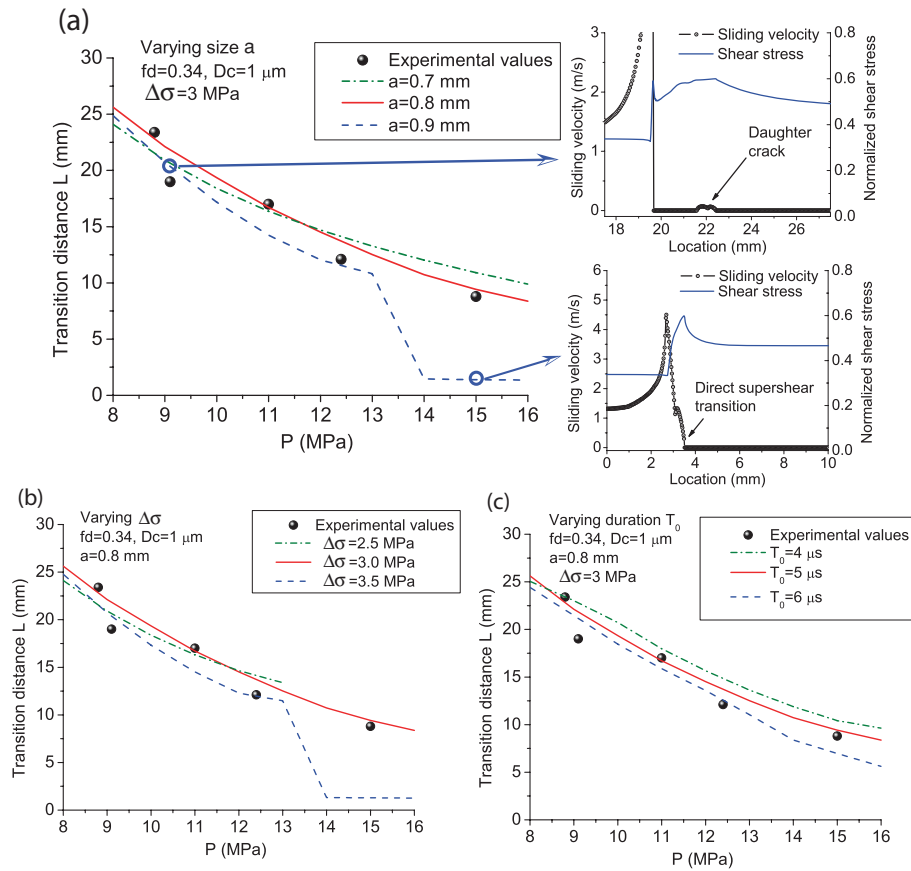


Figure 10. Dependence of transition distances on the parameters of the initiation procedure for the case of $f_d = 0.34$ and pressure-independent $D_c = 1 \mu\text{m}$. The reference set of parameters is that of Fig. 7(a), $a = 0.8 \text{ mm}$, $\Delta\sigma = 3 \text{ MPa}$, $T_0 = 5 \mu\text{s}$. In each panel, one of these parameters is varied and the results are shown for simulations with different values of: (a) the half-size a of the rupture initiation procedure, (b) normal stress reduction $\Delta\sigma$, and (c) duration T_0 . In panel (a), the snapshots of sliding velocity and shear stress for two values of P show that, for $a = 0.9 \text{ mm}$, supershear transition occurs by the Burridge–Andrews mechanism for smaller P and by the direct transition at the rupture tip for larger P .

estimates how long (or developed) the rupture is at the end of the initiation procedure. If the rupture is relatively short at that time, with $c_R T_0 / L_c$ of about 1 or 2, then the initiation region is still a large fraction of the overall rupture length and the rupture has to be vigorous enough to survive the slow-down in the initiation region. That requires a stronger initiation procedure which would also promote the direct supershear transition. That is exactly what happens for the cases in Sections 3.1–3.4 where, depending on the rupture initiation parameters, the rupture either arrests shortly after the end of the initiation procedure or survives but then experiences the direct transition to supershear speeds at the rupture tip. In Sections 4.1–4.3, $c_R T_0 / L_c$ is much larger, more than 3, which means that the crack is well developed at the end of the initiation procedure, and the end of the initiation procedure does not have a significant effect. That allows us to use a more gentle initiation procedure in Sections 4.1–4.2 (with $\Delta\sigma = 3.0 \text{ MPa}$ and not 5 MPa as in Section 3), which leads to sustained rupture propagation but not the direct supershear transition.

Can we distinguish between the two transition mechanisms in the experiments? In Xia *et al.* (2004), the rupture progression was captured by photoelastic images taken every $2 \mu\text{s}$ which, for the rupture propagating close to the Rayleigh wave speed, translates into spatial resolution of the crack tip position of 2 mm . However, the supershear rupture is clearly identifiable on the images only after it generates visible Mach cones, that is, some time after the transition.

Hence it is not easy to distinguish between the daughter crack which nucleates $1\text{--}3 \text{ mm}$ in front of the crack tip and a supershear surge of the main crack tip itself.

A more promising approach is to compare slip velocity histories from simulations and from experiments. These experimental measurements can be done using laser velocimeters (Lykotrafitis *et al.* 2006; Lu *et al.* 2007; Rosakis *et al.* 2007). In particular, Lu *et al.* (2007) recently reported experimental observations of both pulse-like and crack-like ruptures, some of which transitioned to supershear speeds in the time window of the observations. The experimental set-up was the same as in Xia *et al.* (2004) with the addition of laser velocimetry. The experimental conditions such as surface preparation, capacitor discharge etc. were slightly different, potentially resulting in a slightly different static friction coefficient, intensity of the wire explosion, etc. Fig. 11(a) shows one of the experimental slip velocity profiles, measured at the distance of 40 mm from the explosion site, for the inclination angle $\alpha = 30^\circ$ and $P = 14 \text{ MPa}$. The dashed line shows the shear wave arrival at the location. Since the rupture has arrived before the shear waves, we know that the rupture is supershear as it arrives at this location. There is a prominent peak right behind the shear wave arrival. Note the oscillations with the period of about $5 \mu\text{s}$ present in the slip velocity profile; this is likely the 3-D effect of the thickness of the plate (which is 10 mm), perhaps combined with the effect of the finite duration of the wire explosion.

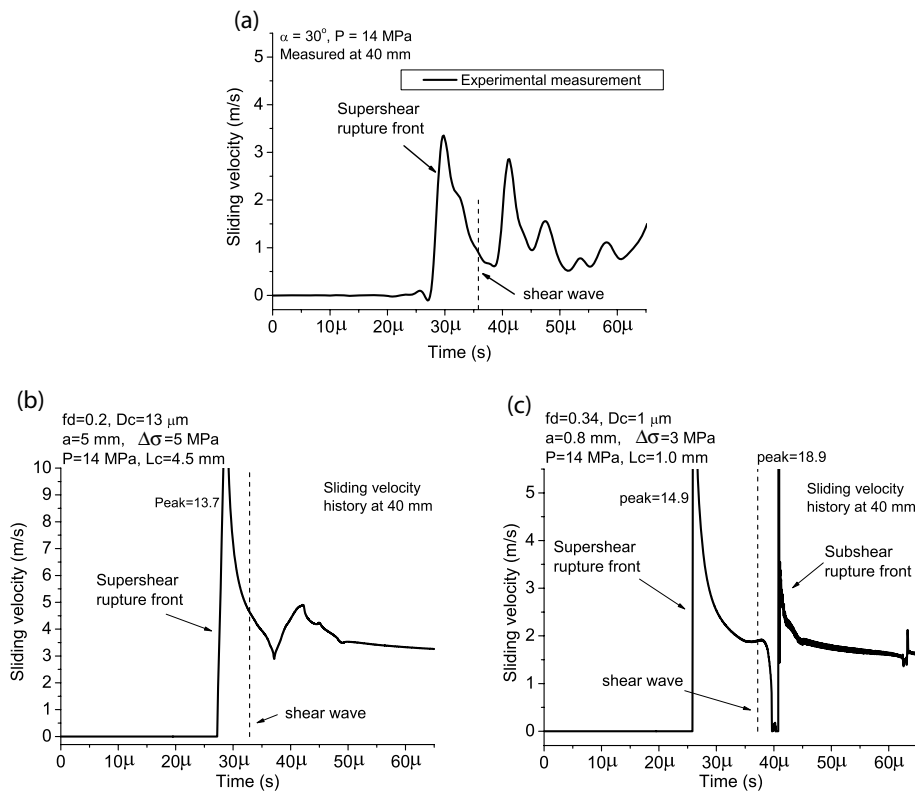


Figure 11. Slip velocity histories at the location of 40 mm along the interface for (a) an experimental measurement of Lu *et al.* (2007), (b) a simulation with the direct supershear transition at the rupture tip and (c) a simulation with the Burridge–Andrews transition mechanism. In all cases, the supershear transition has already occurred, since the rupture tip arrives at this location faster than the shear wave front indicated by the dashed vertical line. Overall, the shape of the slip-velocity profile is similar for all three cases.

How does this profile compare with the ones in our simulations? Fig. 11(b) shows the slip velocity profile for a case from Section 3, with $f_d = 0.2$, $s = 0.5$ and $D_c = 13 \mu\text{m}$, which results in the direct supershear transition at the rupture tip. The overall shape is similar between Figs 11(a) and (b), but the slip velocity values are higher in Fig. 11(b). Although the rupture tip itself has transitioned to supershear speeds, there is still a decrease and increase of slip velocities behind the supershear rupture tip which is the signature of shear and Rayleigh waves that are left behind. Fig. 11(c) shows the slip velocity profile for a case from Section 4, with $f_d = 0.34$, $s = 1.0$ and $D_c = 1 \mu\text{m}$, which results in the mother–daughter crack transition mechanism. Again, the overall shape is similar between Figs 11(a) and (c). The experimental measurements are done on the surface of the sample and at a small distance away from the interface, plus Homalite may exhibit some nonlinear elastic or inelastic behaviour at high slip rates. All these factors would prevent the experiments from recording high slip velocities right at the crack front, or sharp short-lived drops of slip velocity to zero, that are seen in simulations. Other than that, even the level of slip velocities matches in this case, and the simulated profile of Fig. 11(c) has a more pronounced peak behind the shear wave front than that in Fig. 11(b), consistently with the experimental measurement in Fig. 11(a).

Hence both transition mechanisms result in slip velocity profiles that qualitatively match the experimental results. The case with the mother–daughter crack transition does a somewhat better job, although this comparison is necessarily qualitative, since there are a lot of adjustable parameters. However, such comparisons should yield valuable insights when more aspects of the experiments

are quantified (most importantly, the parameters of the initiation procedure).

6 CONCLUSIONS

Motivated by the experiments of supershear transition by Xia *et al.* (2004), we have investigated the effect of a dynamic rupture initiation procedure and fault friction on supershear transition in a plane-stress model with an interface governed by linear slip-weakening friction. To mimic the effects of the wire explosion, our initiation procedure reduces normal stress over a part of the interface for a given time. The values of the static friction coefficient, fault pre-stress, and bulk material properties are well-known for the experimental set up of Xia *et al.* (2004), and we have assumed the corresponding values in this work. However, the dynamic friction properties of the experimental interface and the parameters of the wire explosion are not precisely known, and we have considered several plausible possibilities. While that introduces several adjustable parameters, the requirement that simulations match experimentally observed transition distances for a range of experimental conditions relates parameters to each other and restricts their values.

We find that the dynamic rupture initiation procedure can significantly affect the supershear transition observed in the experiments. First of all, it introduces the possibility of the direct supershear transition at the rupture tip, in which the rupture tip abruptly changes its speed from the values approaching the Rayleigh wave speed to supershear speeds. This direct transition is likely caused by the stressing wave field radiated by the relatively abrupt initiation of

sliding over a part of the interface, and hence it is dominated by the parameters of the initiation procedure. The transition distances for the direct transition are relatively small, 1.5 to 3 L/L_c in the cases we have studied, so that the direct transition occurs soon after the rupture initiation, with no obvious dependence on the value of the seismic ratio s (which determines transition distances in the study of Andrews 1976 and Xia *et al.* 2004, through the mother–daughter crack mechanism). Since the transition distances L in the experiments of Xia *et al.* (2004) varied from 10 to 24 mm for different far-field compressions P , the direct transition mechanism can only be relevant to experiments if the values of the critical crack sizes are 3–8 mm (assuming $L/L_c = 3$ and equal for all P) or larger (assuming $L/L_c < 3$). To initiate spontaneous rupture, the half-size a of the region affected by the wire explosion has to be a significant fraction of L_c . Hence a has to be several mm in this case (in Section 3, the half-size $a = 5$ mm gives a relatively good fit to experimental data). Such values of a require a 0.1-mm wire to significantly affect a much larger region of 10 mm or so.

The Burridge–Andrews mechanism of a supershear daughter crack can still occur for some parameter combinations, although the dynamic initiation procedure significantly shortens, by about 30–50 per cent in the cases we studied, the non-dimensional transition distances L/L_c compared to the study of Andrews (1976) and the calculations of Xia *et al.* (2004) and Rosakis *et al.* (2007), which assumed an initiation procedure representative of a gradually accelerating rupture. This is because the dynamic rupture initiation promotes the development of the shear stress peak in front of the main rupture, which then reaches the static friction threshold for shorter propagation distances in comparison to the above-mentioned studies. Still, the daughter-crack mechanism, even in the presence of the dynamic rupture initiation procedure, can produce much larger values of L/L_c than the direct-transition mechanism, for suitably chosen seismic ratios s . This allows our simulations to match the experimental observations for smaller values of L_c . For example, in Sections 4.1–4.2, we find a good match for $2 L_c$ of the order of 2 mm. This would require that a much smaller extent of the interface affected by the explosion, 2 mm or less (we use the half-size $a = 0.8$ mm in Sections 4.1–4.2), compared with 10 mm for the direct transition ($a = 5$ mm in Section 3).

As mentioned in Section 2, post-experimental surfaces contain a thin layer of metallic debris around the explosion site, which shows how much the material of the wire spread after the explosion. The spatial extent of the layer is typically 4–10 mm along the interface, which would indicate that the half-size a is 2–5 mm. This estimate is broadly consistent with the values of a we have used in Sections 3 and 4. However, it does not provide a firm constraint. On the one hand, one can argue that this estimate may be more of an upper bound, since, in our modelling, $2a$ presents the size of the region that is significantly affected by the explosion, in terms of the resulting normal stress decrease, while the edges of the region covered by the metallic debris may have had only small or negligible normal stress change. This argument would favour smaller values of a , pointing to the parameter regime with the Burridge–Andrews transition mechanism. On the other hand, the size of the particle-covered region may in fact give the value of a more directly, or even underestimate it, which would favour larger values of a as we used in the cases of the direct transition.

In Sections 3 and 4, we have found reasonable parameter regimes that match experimental transition values with both direct supershear transition at the rupture tip and the Burridge–Andrews mechanism, using both pressure-independent and pressure-dependent critical slip D_c . Hence our study shows, in part, that the experimental

results do not necessarily imply the pressure dependence of D_c , once the effect of the rupture initiation procedure is taken into account.

This work underscores the importance of further quantifying experimental parameters for proper interpretation of the experiments and for designing new ones. In particular, the time- and space-dependent effects of the wire explosion need to be determined, and such study is our first priority. It is possible that the wire explosion temporarily opens a part of the interface, a factor not considered in this study. It is also possible and even likely, based on the study of Lu *et al.* (2007), that the interface friction is better described by a rate- and state-dependent law with significant rate-dependence at high slip rates rather than a linear slip-weakening law used in this work. We plan to incorporate these effects into our future modelling.

ACKNOWLEDGMENTS

NL gratefully acknowledges the support of NSF (Grant EAR 0548277) for this study. AJR gratefully acknowledges the support of NSF (Grant EAR 0207873), the US Department of Energy (Grant DE-FG52-06NA 26209) and MURI (Grant N000140610730, Dr Y.D.S. Rajapakse, Program Manager). The numerical simulations for this research were performed on Caltech Division of Geological and Planetary Sciences Dell cluster. We thank Kaiwen Xia for helpful discussions.

REFERENCES

- Aagaard, B.T. & Heaton, T.H., 2004. Near-source ground motions from simulations of sustained intersonic and supersonic fault ruptures, *Bull. Seism. Soc. Am.*, **94**, 2064–2078.
- Abraham, F.F. & Gao, H., 2000. How fast can cracks propagate? *Phys. Rev. Lett.*, **84**, 3113–3116.
- Ampuero, J.-P. & Ben-Zion, Y., 2008. Cracks, pulses and macroscopic asymmetry of dynamic rupture on a bimaterial interface with velocity-weakening friction, *Geophys. J. Int.*, **173**, 674–692.
- Andrews, D.J., 1976. Rupture velocity of plane strain shear cracks, *J. geophys. Res.*, **81**, 5679–5687.
- Archuleta, R.J., 1984. A faulting model for the 1979 Imperial-Valley earthquake, *J. geophys. Res.*, **89**, 4559–4585.
- Bernard, P. & Baumont, D., 2005. Shear Mach wave characterization for kinematic fault rupture models with constant supershear rupture velocity, *Geophys. J. Int.*, **162**, 431–447.
- Bhat, H.S., Dmowska, R., King, G.C.P., Klinger, Y. & Rice, J.R., 2007. Off-fault damage patterns due to supershear ruptures with application to the 2001 M/sub w/ 8.1 Kokoxili (Kunlun) Tibet earthquake, *J. geophys. Res., B, Solid Earth*, **112**, 1–19.
- Bouchon, M. & Vallee, M., 2003. Observation of long supershear rupture during the magnitude 8.1 Kunlunshan earthquake, *Science*, **301**, 824–826.
- Bouchon, M.S., Bouin, M., Karabulut, H., Toksoz, M., Dieterich, M. & Rosakis, A., 2001. How fast is rupture during an earthquake? New insights from the 1999 Turkey earthquakes, *Geophys. Res. Lett.*, **28**, 2723–2726.
- Broberg, K.B., 1989. The near-tip field at high crack velocities, *Int. J. Fract.*, **39**, 1–13.
- Burridge, R., 1973. Admissible speeds for plane-strain self-similar shear cracks with friction but lacking cohesion, *Geophys. J. R. Astro. Soc.*, **35**, 439–455.
- Burridge, R., Conn, G. & Freund, L.B., 1979. Stability of a rapid mode-II shear crack with finite cohesive traction, *J. geophys. Res.*, **84**, 2210–2222.
- Dally, J.W. & Riley, W.F., 1991. *Experimental Stress Analysis*, McGraw-Hill, New York.
- Das, S., 2007. The need to study speed, *Science*, **317**, 905–906.
- Das, S. & Aki, K., 1977. Numerical study of 2-dimensional spontaneous rupture propagation, *Geophys. J. R. Astro. Soc.*, **50**, 643–668.
- Day, S.M., 1982. 3-Dimensional simulation of spontaneous rupture - the effect of nonuniform prestress, *Bull. Seismol. Soc. Am.*, **72**, 1881–1902.

- Dunham, E.M., 2007. Conditions governing the occurrence of supershear ruptures under slip-weakening friction, *J. geophys. Res.*, **112**, B07302, doi:10.1029/2006JB004717.
- Dunham, E.M. & Archuleta, R.J., 2004. Evidence for a supershear transient during the 2002 Denali fault earthquake, *Bull. seism. Soc. Am.*, **94**, S256–S268.
- Dunham, E.M. & Archuleta, R.J., 2005. Near-source ground motion from steady state dynamic rupture pulses, *Geophys. Res. Lett.*, **32**, L03302.
- Ellsworth, W.L. *et al.*, 2004. Near-field ground motion of the 2002 Denali fault, Alaska, earthquake recorded at Pump Station 10, *Earthq. Spect.*, **20**, 597–615.
- Festa, G. & Vilotte, J.P., 2006. Influence of the rupture initiation on the intersonic transition: crack-like versus pulse-like modes, *Geophys. Res. Lett.*, **33**, L15320.
- Freund, L.B., 1979. Mechanics of dynamic shear crack propagation, *J. geophys. Res.*, **84**, 2199–2209.
- Gao, H., Huang, Y. & Abraham, F.F., 2001. Continuum and atomistic studies of intersonic crack propagation, *J. Mech. Phys. Solids*, **49**, 2113–2132.
- Geubelle, P.H. & Kubair, D.V., 2001. Intersonic crack propagation in homogeneous media under shear-dominated loading: numerical analysis, *J. Mech. Phys. Solids*, **49**, 571–587.
- Geubelle, P.H. & Rice, J.R., 1995. A spectral method for three-dimensional elastodynamic fracture problems, *J. Mech. Phys. Solids*, **43**, 1791–1824.
- Liu, Y. & Lapusta, N., 2008. Transition of mode II cracks from sub-Rayleigh to intersonic speeds in the presence of favorable heterogeneity, *J. Mech. Phys. Solids*, **56**, 25–50.
- Lu, X., Lapusta, N. & Rosakis, A.J., 2007. Pulse-like and crack-like ruptures in experiments mimicking crustal earthquakes, *Proc. Natl. Acad. Sci. U.S.A.*, **104**, 18 931–18 936.
- Lykotrafitis, G., Rosakis, A.J. & Ravichandran, G., 2006. Self-Healing pulse-like shear ruptures in the laboratory, *Science*, **313**, 1765–1768.
- Madariaga, R. & Olsen, K.B., 2000. Criticality of rupture dynamics in 3-D, *Pure Appl. Geophys.*, **157**, 1981–2001.
- Needleman, A. & Rosakis, A.J., 1999. The effect of bond strength and loading rate on the conditions governing the attainment of intersonic crack growth along interfaces, *J. Mech. Phys. Solids*, **47**, 2411–2449.
- Ohnaka, M., 2003. A constitutive scaling law and a unified comprehension for frictional slip failure, shear fracture of intact rock, and earthquake rupture, *J. Geophys. Res.-Solid Earth*, 108, 2080.
- Olsen, K.B., Madariaga, R. & Archuleta, R.J., 1997. Three-dimensional dynamic simulation of the 1992 Landers Earthquake, *Science*, **278**, 834–838.
- Robinson, D.P., Brough, C. & Das, S., 2006. The M-w 7.8, 2001 Kunlunshan earthquake: extreme rupture speed variability and effect of fault geometry, *J. geophys. Res.*, **111**, B08303.
- Rosakis, A.J., 2002. Intersonic shear cracks and fault ruptures, *Adv. Phys.*, **51**, 1189–1257.
- Rosakis, A.J., Samudrala, O. & Coker, D., 1999. Cracks faster than the shear wave speed, *Science*, **284**, 1337–1340.
- Rosakis, A.J., Xia, K.W., Lykotrafitis, G. & Kanamori, H., 2007. Earthquake seismology dynamic shear rupture in frictional interfaces: speeds, directionality and modes, in *Treatise in Geophysics*, eds Schubert, G. & Kanamori, H., Elsevier Amsterdam.
- Shi, Z.Q., Ben-Zion, Y., 2006. Dynamic rupture on a bimaterial interface governed by slip-weakening friction, *Geophys. J. Int.*, **165**, 469–484.
- Shi, Z.Q., Ben-Zion, Y. & Needleman, A., 2008. Properties of dynamic rupture and energy partition in a solid with a frictional interface, *J. Mech. Phys. Solids*, **56**, 5–24.
- Xia, K.W., Rosakis, A.J. & Kanamori, H., 2004. Laboratory earthquakes: the sub-Rayleigh-to-supershear rupture transition, *Science*, **303**, 1859–1861.